Selective Transition Enhancement in a *g*-Engineered Diradical

Joe Komeda,[a] Athanassios K. Boudalis,*[b, c] Nicolas Montenegro-Pohlhammer,[d] Cyril Antheaume,[c] Asato Mizuno,*[e] Philippe Turek,[b] and Mario Ruben*[a, c, f]

A diradical with engineered *g*-asymmetry was synthesized by grafting a nitroxide radical onto the $[Y(Pc)_2]^\bullet$ radical platform. Various spectroscopic techniques and computational studies revealed that the electronic structures of the two spin systems remained minimally affected within the diradical system. Fluid-solution Electron Paramagnetic Resonance (EPR) experiments revealed a weak exchange coupling with $|J| \sim 0.014$ cm^{-1}, subsequently rationalized by CAS-SCF calculations. Frozen solution continuous-wave (CW) EPR experiments showed a complicated and power-dependent spectrum that eluded analysis using the point-dipole model. Pulse EPR manipulations with varying microwave powers, or under varying magnetic fields, demonstrated that different resonances could be selectively enhanced or suppressed, based on their different tipping angles. In particular, Field-Swept Echo-Detected (FSED) spectra revealed absorptions of MW power-dependent intensities, while Field-Swept Spin Nutation (FSSN) experiments revealed two distinct Rabi frequencies. This study introduces a methodology to synthesize and characterize *g*-asymmetric two-spin systems, of interest in the implementation of spin-based CNOT gates.

1. Introduction

In the quest for systems that can implement qubits satisfying DiVicenzo's criteria,[1] molecular spin qubits have arisen as promising candidates, since their chemical structures can be fine-tuned and since they can be positioned with atomic

[a] J. Komeda, M. Ruben
Institute of Nanotechnology (INT) Karlsruhe Institute of Technology (KIT) Hermann-von-Helmholtz-Platz 1, 76344 Eggenstein-Leopoldshafen (Germany)
E-mail: mario.ruben@kit.edu

[b] A. K. Boudalis, P. Turek
Institut de Chimie de Strasbourg (UMR 7177, CNRS-Unistra), Université de Strasbourg, 4 rue Blaise Pascal, CS 90032, F-67081 Strasbourg, France
E-mail: bountalis@unistra.fr

[c] A. K. Boudalis, C. Antheaume, M. Ruben
Centre Européen de Sciences Quantiques (CESQ) within the Institut de Science et d'Ingénierie Supramolaiculaires – ISIS, 8 allée Gaspard Monge, BP 70028, F-67083 Strasbourg Cedex, France

[d] N. Montenegro-Pohlhammer
Centro Integrativo de Biología y Química Aplicada (CIBQA), Universidad Bernardo O'Higgins, General Gana 1702, Santiago, 8370854, Chile

[e] A. Mizuno
Division of Chemistry, Department of Materials Engineering Science, Graduate School of Engineering Science, Osaka University, 1-3 Machika-neyama, Toyonaka, Osaka 560-8531, Japan
E-mail: mizuno.asato.es@osaka-u.ac.jp

[f] M. Ruben
Institute of Quantum Materials and Technologies (IQMT) Karlsruhe Institute of Technology (KIT) Hermann-von-Helmholtz-Platz 1 76344 Eggenstein-Leopoldshafen (Germany)

precision.[2–4] Their decoherence times are sufficiently long, with a record phase-memory time (T_m) of 670 μs being reported for a V^{IV} $S = 1/2$ system,[5] which is comparable to those of super-conducting qubits, the benchmark of qubit studies. While the studies on molecular qubits have focused mostly on metal complexes for the past three decades, organic radicals have increased their presence due to their unique properties.[6–8] Their low spin-orbit couplings induce weaker interactions with their lattice, which increases their spin-lattice relaxation times (T_1). Since T_1 constitutes an upper limit for T_m, long T_1 extends the possibilities for their practical use. Moreover, their structural tunability enables the construction of multi-qubit arrays.

Recently, this research has tackled another very important problem, the implementation of two-qubit gates, a *sine qua non* for the construction of a universal set of the quantum gates and the practical implementation of quantum computation.[1,9] In that context, organic radicals have been shown to be suitable platforms for such implementations. Indeed, a diradical exhibiting only a weak intramolecular dipolar interaction, is characterized by a singlet state denoted $|10\rangle$, and by a triplet consisting of three sublevels denoted $|00\rangle$, $|01\rangle$, and $|11\rangle$. The allowed intratriplet EPR transition $|00\rangle \rightarrow |01\rangle$ can then encode the operation of a CNOT gate, while the flip-flop $|10\rangle \rightarrow |01\rangle$ transition could encode the SWAP gate. This was proposed theoretically by Volkov and Salikhov[10] and tested experimentally by Nakazawa et al..[11] Subsequently, the concept was extended to photogenerated diradicals[7] and recently a protocol for the entanglement of two spins of a diradical was demonstrated.[12]

Over the past decade, we have investigated the utility of the bis(phthalocyaninato)terbium(III) ($[Tb(Pc)_2]^\bullet$) double-decker complex as a spin qubit, using its nuclear spin (^{159}Tb: $I = 3/2$) to encode information. Despite the difficulties in measuring and manipulating nuclear spin, we have demonstrated read-out and manipulation of nuclear spin states of $[Tb(Pc)_2]^\bullet$, by spin

Chemistry–A European Journal

Research Article
doi.org/10.1002/chem.202400420

Chemistry Europe
European Chemical
Societies Publishing

transport measurements under magnetic fields and microwave irradiation of $[Tb(Pc)_2]^\bullet$ attached to the electrodes.[13,14] More recently, we have shown the first experimental implementation of Grover's algorithm (a quantum search algorithm) based on the multi-level nuclear spin system of the ^{159}Tb nucleus.[15] In the spin transport measurement, the radical delocalized over the phthalocyanine rings of $[Tb(Pc)_2]^\bullet$ (S_{Pc}) takes the precise role which serves as a spin cascade for the detection of the nuclear spin states. On the other hand, bis(phthalocyaninato)yttrium(III) double-decker complex $[Y(Pc)_2]^\bullet$ (**1**) with a diamagnetic

yttrium(III) ion garnered substantial interest since S_{Pc} can be isolated as a pure radical. We have recently reported the room-temperature coherent spin manipulation of a magnetically condensed phase of **1** in the solid state using pulsed Electron Paramagnetic Resonance (EPR) spectroscopy (Figure 1, top).[16]

The structural tunability of **1** derivatives prompted us to consider it as a platform for the construction of CNOT gates mediated through dipolar interactions between two electron spins. In previous work, we developed molecular-engineered sandwich type complexes similar to **1** with one Pc substituted by a porphyrin ($[Y(Pc)(por)]^\bullet$) tethered to another one to construct double-decker dimers ($[Y(Pc)(por)]^\bullet$–$[Y(Pc)(por)]^\bullet$, Figure 1, middle).[17] Pulse EPR studies revealed long T_1 and T_M times, similar to that of **1**, confirming that such relaxation characteristics are retained in the mixed-ligand complexes. Even though this tethered diradical may constitute a two-qubit system, the presence of identical and isotropic g-tensors hampers each qubit's selective addressing.

Based on these observations we were motivated to design diradicals with engineered g-asymmetry based on the $[Y(Pc)_2]^\bullet$ platform. Herein, we report on the design and preparation of the radical-functionalized double-decker phthalocyanine complex, **2** (Figure 1 bottom, Figure 2a), a novel asymmetric two-qubit system in which the $[Y(Pc)_2]^\bullet$ skeleton is functionalized with an isoindoline-based nitroxide radical moiety ($[NO]^\bullet$).

As will be shown, the interspin distance and the strength of the exchange interaction within diradicals are critical parame-
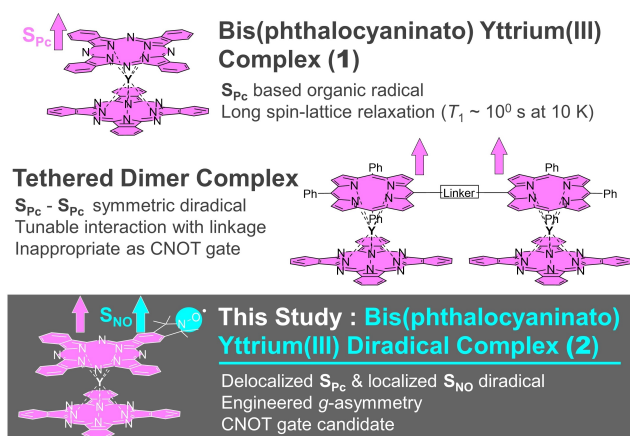

Figure 1. Overview of the studies on yttrium(III) bis(phthalocyaninato) or (phthalocyaninato)(porphyirinato) complexes.
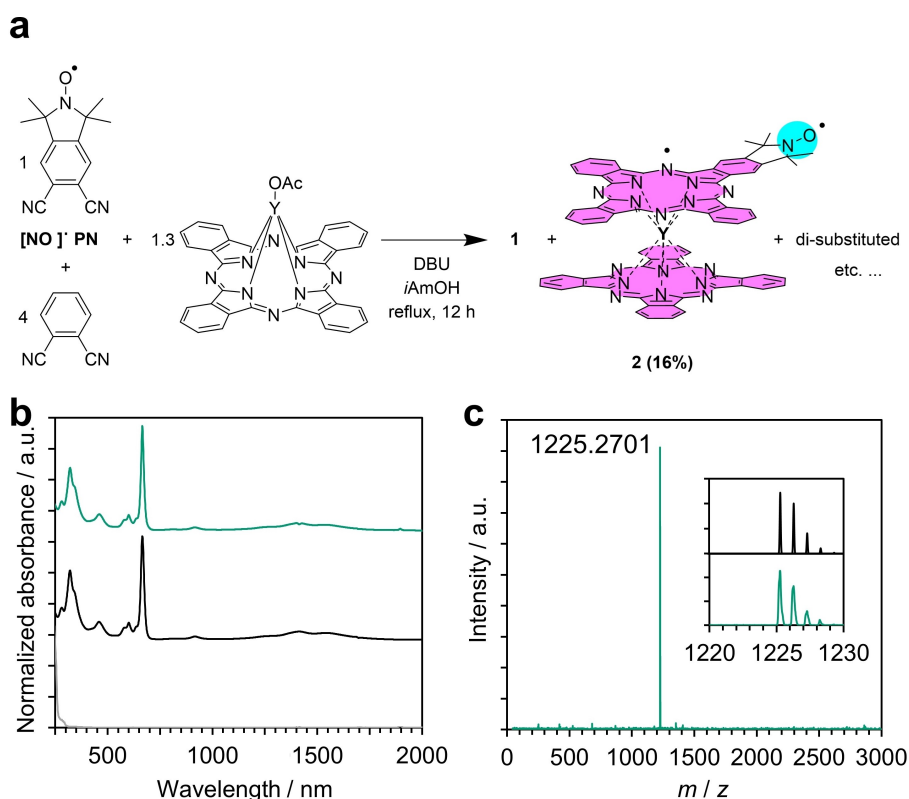
a

b **c**

Figure 2. (a) Reaction scheme for the preparation of **2**. In the molecular structure of **2**, S_{Pc}, which is delocalized over phthalocyanine rings, is depicted in magenta; S_{NO}, which is localized at $[NO]^\bullet$, is represented as a cyan circle. (b) UV-vis-NIR absorption spectra of **2** (green) and **1** (black) in CH_2Cl_2. (c) ESI-MS spectrum of **2**. The inset compares the experimental (green) and simulated (black) isotopic patterns.

Chemistry–A European Journal

Research Article
doi.org/10.1002/chem.202400420

Chemistry
Europe
European Chemical
Societies Publishing

ters, which can lead to two limiting cases that may be of interest in Quantum Information Processing. In the case of a very weak coupling a two-qubit gate may be implemented, such as CNOT, and in the case of a strong coupling a qutrit may implemented within the spin triplet ($S=1$) state of the diradical.

2. Results

2.1. Synthesis and Characterization

The isoindoline-based nitroxide radical was chosen as the peripheral radical group because of its stability against the harsh conditions of phthalocyanine formation reaction.[18] Moreover, its rigid structure is preferable to maintain a fixed orientation and distance of the two radicals (S_{pc} and S_{NO}) in the double-decker-complex, without any rotation of the radical moiety in solution. Previously, mono-, di-, tri- substituted $[Ln(Pc)_2]^•$ analogues were reported to be obtained in better yield in the reactions between phthalonitrile derivatives and lanthanide mono-phthalocyanine complex than in the other conventional synthetic methods for $[Ln(Pc)_2]^•$ analogues.[19–21] Accordingly, we employed this method using yttrium(III) phthalocyaninato acetate complex (YPcOAc) as a template to synthesize **2**; a radical-functionalized phthalonitrile, 5,6-Dicyano-1,1,3,3-tetramethylisoindolin-2-yloxyl ($[NO]^•PN$) and YPcOAc were prepared according to the literature methods.[18,22–24] Then, the reaction of $[NO]^•PN$ with a slight excess of phthalonitrile and YPcOAc in the presence of 1,8-diazabicyclo- [5.4.0]undec-7-ene (DBU) resulted in the mixture of **1**, **2**, di-substituted $[Y(Pc)_2]^•$, and other unidentified by-products (Figure 2). The reaction mixture was purified by silica gel column chromatography, which was repeated several times until only one green spot appeared in thin-layer chromatography (TLC), followed by reprecipitation from a CHCl$_3$/MeOH mixture to obtain diradical $[Y(Pc)(PcNO)]^{••}$ (**2**) as a green powder. Unfortunately, in any combination of conventionally used solvents such as CH$_2$Cl$_2$, hexane, etc., the material didn't crystalize. To our best knowledge, no single-crystal structure has been reported for mono-substituted asymmetric $[Ln(Pc)_2]^•$ derivatives.

The obtained material was characterized with various spectroscopic methods. The UV-Vis-NIR absorption spectrum of **2** is quite similar to that of **1**, showing a Soret band around 350 nm and a Q band at around 750 nm (Figure 2b), characteristic of bis-(phthalocyaninato) complexes (Figure S2a). Absorption bands that represent S_{pc} were detected as well; a BV band (ca. 450 nm), a RV band (ca. 900 nm), and an intervalence band at the NIR. To elucidate the reason for the absence of the characteristic peak of the $[NO]^•$ moiety in the spectrum of **2**, UV-vis-NIR absorption spectroscopy and TD-DFT calculation were performed on $[NO]^•PN$ (Figure S2). In the UV-vis spectrum, no peak stronger than absorption coefficients (ε) of 0.5 M^{-1}cm^{-1} was calculated in the region $\lambda > 300$ nm. Furthermore, TD-DFT calculation predicted that two absorption peaks involved in the $[NO]^•$ moiety were located at $\lambda = 484.72$ and 401.81 nm, whose oscillation strengths were much weaker than those of the peaks in the UV region. Therefore, the UV-vis absorption spectrum

and TD-DFT calculation of $[NO]^•PN$ support that the absorption bands corresponding to the $[NO]^•$ moiety are negligibly weak ($\varepsilon < 0.5$ M^{-1}cm^{-1}) compared with that of Q band of LnPc$_2$ (ε ~2×10^5 M^{-1}cm^{-1})[25]), which thereby dominate the spectrum of **2**.

In the IR spectra, at 500–1000 cm^{-1} similar peaks were observed for **2** and $[NO]^•PN$, while around 1500 cm^{-1} similar peaks were observed for **2** and **1** (Figure S2b). The peak at 1700 cm^{-1} was observed for both **2** and $[NO]^•PN$, which is characteristic of isoindoline nitroxide.[18] On the other hand, no peak was observed around 3500 cm^{-1} for **2**, which certifies the absence of O–H bonds.

High-resolution Electrospray Ionization Mass Spectrometry (ESI-HRMS) was performed for **2** (KIT) and showed a signal from one ion, whose isotopic pattern matched well with the calculated one (Figure 2c). These results were fully consistent to ESI-HRMS studies ran on the EPR sample (Figure S3, ISIS). In addition, to fully determine the stability of **2** with respect to protonation, an ESI-HRMS spectrum with an addition of 0.1%(v/ v) of acetic acid in MeOH was recorded. This showed a peak shift of m/z by $+1$ for a fraction of the sample (Figure S4), consistent with disproportionation of the nitroxide moieties into hydroxide and oxoammmonium species in acidic media.[26] A significant fraction of the sample resisted protonation even under those conditions, further demonstrating the stability of the $[NO]^•$ radical of **2**.

During EPR spectroscopy in fluid solution, a minor (~10%) nitroxyl-radical component was detected (vide infra). UV-Vis-NIR measurement on the EPR sample identified the minor component as oxidized **2** formulated as $[Y(Pc)(PcNO)]^{•+}$ (**2′**, Figure S5b). The absence of the characteristic shoulder in the as-prepared sample (see Figure 2b) and its presence in the spectrum of the EPR sample (see Section 2.3 in the Supporting Information), indicate its formation due to slow oxidation of **2** during sample storage and/or preparation. We note that ESI-HRMS studies on the EPR sample was inherently unsuitable for its detection, as the technique is based on ionization of **2** to **2′** and detection of the latter.

2.2. Computational and Electrochemical Study

Through Density Functional Theory (DFT) and Wave Function (WFT) based calculations, we determined the molecular and electronic structure of **2** and, in addition, the nature of the magnetic coupling between the unpaired electron localized at $[NO]^•$ group and the one on the Pc rings.

Energy calculations revealed that the MOs of **2** are quite similar and energetically close to those of **1**, except for SOMO-1 of **2**, which is localized at the $[NO]^•$ moiety (Figure S6). This result agrees with the result of UV-Vis-NIR absorption spectroscopy and cyclic voltammogram study (Figure 2b and Figure 3, respectively). The coupling constant J was calculated as 4.24 cm^{-1} (127 GHz) by a BS methodology, while a CASSCF/ NEVPT2 methodology yielded a value of -0.04 cm^{-1} (1.2 GHz). Keeping in mind that the assignment of the sign of J is quite challenging, the magnitude of the latter value is in good
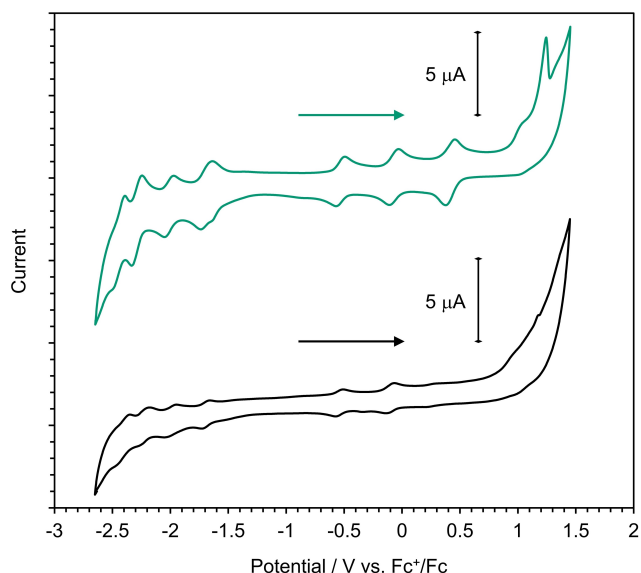
Figure 3. Cyclic voltammogram of **2** (green) and **1** (black) at a scan rate of 100 mVs⁻¹. The directions were shown by arrows.

agreement with the experimental value derived from fits of fluid solution EPR spectra (vide infra). The complete study, as well as the technical details can be found in Section 3 of the Supporting information.

To study the redox properties of **2**, cyclic voltammetry was performed on **1** and **2**. The cyclic voltammogram of **2** is quite similar to that of **1** except for additional features characteristic of the nitroxide moiety: **2** exhibited seven redox couples similar to those for **1**, which can be assigned to the oxidation ($E^{0\prime} =$ 1.04 and -0.07 V vs. ferrocenium/ferrocene (Fc⁺/Fc)) and reduction ($E^{0\prime} = -0.53, -1.69, -2.01, -2.29$, and -2.44 V) of the Pc ligands (Table S2).[27,28] On the other hand, the irreversible oxidation wave at 1.25 V and the redox couple of $E^{0\prime} = 0.43$ V were only observed with **2**. To identify these waves, cyclic voltammetry was also conducted on [NO]• dibromobenzene (**SM3**; Figure S10 and Table S3). It showed an irreversible wave at 1.53 V, as well as a redox couple at $E^{0\prime} = 0.53$ V, which is consistent with previously reported values.[29] By taking into account that the redox potential differs with various functional groups (0.37–0.53 V), these waves are assigned to the oxidations centered at [NO]• moiety. Therefore, the redox property of **2** is characterized as the sum of redox properties of [Y(Pc)₂]• and [NO]• moieties. This result is consistent with the result of DFT calculation, where MOs of **2** are separated into two; ones localized on [Y(Pc)₂]• moiety, which is quite similar to MOs of **1**, and the others localized on [NO]• moiety. (Figure S6).

2.3. Determination of the J-Coupling with CW EPR

Room-temperature CW spectra in fluid solution were recorded to reveal the isotropic part of the hyperfine interactions. These reveal two clearly defined components, each characterized by triplet signals, typical of hyperfine coupling to ¹⁴N ($I = 1$) and are shown in Figure 4, top.
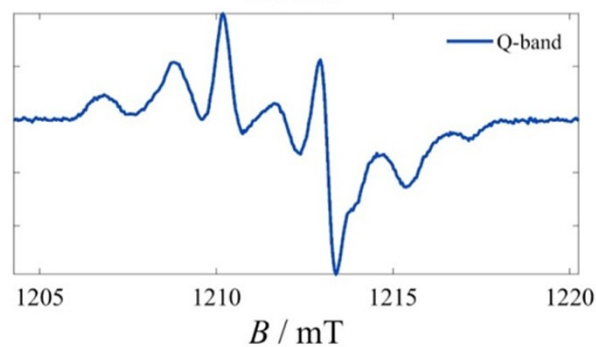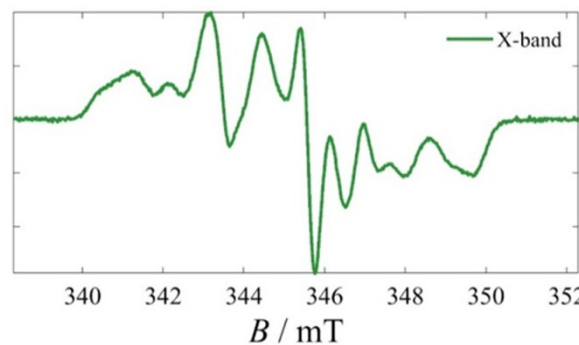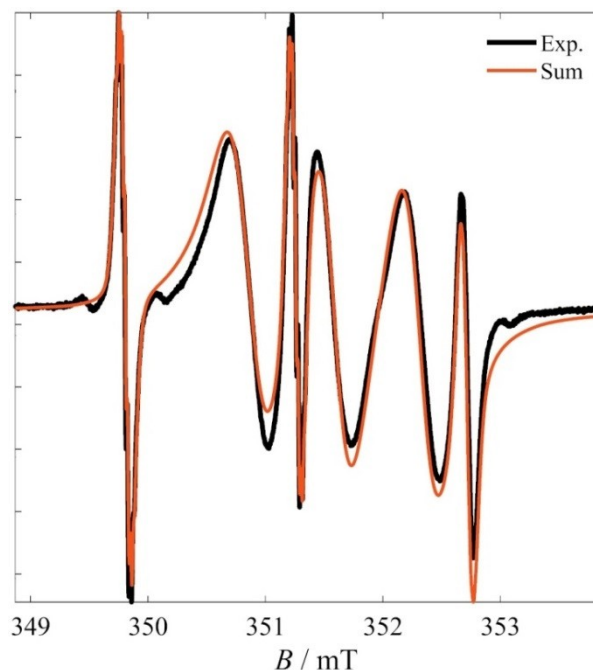

Figure 4. Top: X-band fluid solution spectrum (black) in 4:1 CD_2Cl_2:$CHCl_3$ at ambient temperature and simulation (red) as the mixture of non-interacting nitroxide **2'** (~10%) and spin-coupled complex **2** with $J = 15$ mT (~90%). Experimental conditions: $f_{EPR} = 9.8620$ GHz, $\Delta B_{mod} = 0.0098$ mT_{pp}, $P_{MW} = 0.51$ mW. **Middle-bottom**: X- and Q-band CW EPR spectra on a frozen solution of **2**. Experimental conditions: X-band. $T = 90$ K, $f_{EPR} = 9.67629$ GHz, $\Delta B_{mod} = 0.1$ mT_{pp}, $P_{MW} = 0.52$ μW. Q-band. $T = 85$ K, $f_{EPR} = 34.0002$ GHz, $\Delta B_{mod} = 0.1$ mT_{pp}, $P_{MW} = 1.12$ μW.

In preliminary fits, each of these components was considered separately and fitted with Easyspin's garlic function. One component, (subsequently assigned to the diradical system, see below) was characterized by large line widths, whereas the other (subsequently assigned to a [Y(Pc)(PcNO)]•⁺ monoradical,

Chemistry–A European Journal

Research Article
doi.org/10.1002/chem.202400420

Chemistry
Europe
European Chemical
Societies Publishing

see below) consisted of narrow lines with additional features attributed to ^{1}H and ^{13}C hyperfine couplings. The best-fit parameters were: $g_{dirad} = 2.0041$, $\sigma_G = 0.201$ mT$_{pp}$, $\sigma_L = 0.203$ mT$_{pp}$, $A_{Ndirad} = 20.47$ MHz, with a relative weight of 92% and $g_{NO} = 2.0060$, $\sigma_G = 0.013$ mT$_{pp}$, $\sigma_L = 0.020$ mT$_{pp}$, $A_{N(NO)} = 40.96$ MHz, $A_{H(NO)} = 0.69$ MHz, $A_{C(NO)} = 17.88$ MHz, with a relative weight of 8%. The spin Hamiltonian parameters for the nitroxide radical are strikingly close to the ones previously determined for the parent 1,1,3,3-tetramethylisoindolin-2-yloxy radical from a 218 K fluid toluene solution, i.e. $g_{NO} = 2.0054$, $A_{N(NO)} = 39.52$ MHz, $A_{H(NO)} = 0.68$ MHz, $A_{C(NO)} = 17.9$ MHz.[30] The fitting results are shown in Figure S11.

An intriguing aspect of these spectra was the hyperfine splittings, which had not been detected in the powder and frozen solution spectra of the parent 1,[16,17] and which were not predicted by DFT calculations either. To fully confirm that this is also the case in fluid solution spectra of the parent molecule, such studies were carried out on 1. These demonstrated a simple singlet signal, lacking any hyperfine splitting. Best-fit parameters were $g_{pc} = 2.0022$, $\sigma_G = 0.462$ mT$_{pp}$, $\sigma_L = 0.027$ mT$_{pp}$ (Figure S12).

So while one set of signals was strikingly similar to those of the free nitroxide radical, the other was distinctly different from the spectra of the parent 1. This prompted us to consider that the broad triplet belongs to the diradical 2, whereas the narrow radical belongs to a minority monoradical [Y(Pc)(PcNO)]$^{\bullet+}$ species (2′), with a radical present only on the nitroxide moiety. Such a species would be indistinguishable from ESI-MS spectra of the diradical, while the existence of a small amount (less than 10%) of the oxidized species of 2 was indicated by UV-vis-NIR absorption spectrum of 2 used for EPR (see Figure S5 and the following sentence).

The fluid solution spectrum of 2 was simulated with the program CUNO that includes electron spin-spin coupling between two inequivalent $S = 1/2$ centers.[31] Incomplete motional averaging is approximated with the Kivelson model that was developed for nitroxide radicals.[32] The sharp lines at 349.81, 351.26, and 352.72 mT with partially resolved proton hyperfine coupling are assigned to 2′ in which the Pc ring system is diamagnetic. The parameters for the non-interacting nitroxide were $g_{NO} = 2.0060$, $A_N = 40.74$ MHz, A_H (12 protons) = 0.67 MHz, and Kivelson linewidth parameters $A = 0.028$ mT, $B = 0.006$ mT. These values are in good agreement with the above mentioned fits and the corresponding values of the structurally related free radical.[30] The broad lines are assigned to the spin-coupled 2 diradical which was simulated with $g_{NO} = 2.0060$, $A_N = 40.74$ MHz, A_H (12 protons) = 0.67 MHz, $g_{pc} = 2.0023$, $J = 0.014$ cm^{-1} (420 MHz), and Kivelson linewidth parameters $A = 0.33$ mT, $C = 0.001$ mT. These parameters are in good agreement with expectations for the two paramagnetic centers in the absence of spin-spin interaction. In addition, the J value is in close agreement with the one computed through WFT based calculations ($|J| = 0.04$ cm^{-1}, see section 3.3 in the SI). The simulation does not include the natural abundance ^{13}C hyperfine lines. Similarly good agreement between simulation and experiment could be obtained with larger values of J, but not with J less than about 336 MHz (0.011 cm^{-1}). A discussion of the

dependence of line positions on J is given in the supplementary materials (Section 5.2).

These results were taken into account in the further treatment of CW EPR spectra of frozen solutions of the diradical (see below).

To determine the magnetic anisotropies in the diradical system, CW EPR spectra were recorded in frozen solutions at X and Q-bands. These revealed a complicated spectrum indicative of the involvement of several spin Hamiltonian terms (Figure 4, middle and bottom).

Variable-power studies at 90 K demonstrated different changes in the intensities of different resonances. Indeed, the intensities of the high-field resonances ($g < 2.002$) increased more than those at lower fields upon increase of the microwave power. This severely changed the shape of the spectrum, thus introducing uncertainties in the attempted fits. The entire spectrum also demonstrated saturation effects down to very low MW powers, as demonstrated by plots scaled to $\sqrt{P_{MW}}$ (see Figure S14).

Attempts were made to fit these spectra to a model comprising two $S = 1/2$ spins interacting through the exchange interaction derived above and a dipolar interaction assuming a point-dipole approximation. These attempts failed, which we attribute to the inadequacy of the point-model in reproducing the behavior of so closely spaced spins, one of which is strongly delocalized. These attempts are described extensively in the SI.

2.4. Selective Resonance Enhancement via Pulse-EPR Experiments

A first interpretation of the CW spectra behavior, considered different relaxation profiles of the two spin centers. To circumvent passage effects related to slow spin-lattice relaxation, we undertook field-sweep echo-detected (FSED) pulsed EPR experiments which permit an appropriate choice of Shot Repetition Times (SRT) by prior measurement of T_1 (SRT > 5T_1).

Notably, FSED and CW spectra revealed marked differences (see Figure S16). To understand their origins we undertook field-dependent saturation-recovery and echo-decay experiments to assess the spin dynamics of each resonance (Figures S19 and S20). In particular, we sought to determine: (a) whether T_1 and T_M exhibited anisotropies, and (b) whether the two spins, S_{pc} and S_{NO}, exhibited individual relaxation profiles, or whether they behaved as a unique magnetic system.

For the analysis of these experiments two approaches were taken. First, the saturation-recovery (or echo decay) trace was fitted to a monoexponential recovery (or decay), allowing us to assess T_1 (or T_M) field dependences. Second, to unequivocally establish whether unique relaxation times suffice to describe the experimental time traces, we undertook inverse Laplace transforms (LT^{-1}) at each field (see SI for details), a mathematical treatment previously applied in REFINE spectroscopies.[33,34]

Either method convincingly demonstrated unique T_1 and T_M times of the spin dynamics of all resonances, as well as weak anisotropies. In particular, the T_1 field dependence is similar to that previously observed in nitroxide radicals,[35] suggesting that

the faster-relaxing component (i.e. the nitroxide radical in the current case) accelerates the relaxation of the slow-relaxing component (i.e. the $[Y(Pc)_2]^\bullet$ radical)] in the coupled diradical system. Indeed, this was previously observed in nitroxide-trityl exchange-coupled diradicals,[36] with the faster-relaxing nitroxide becoming the rate-determining component of the coupled system, accelerating the relaxation of the trityl component.

Overall, variable-field experiments demonstrated the uniqueness of relaxation rates, demonstrating the presence of a unique exchange-coupled system in **2**, whose magnetic relaxation is determined by its faster-relaxing nitroxide sub-component, including its characteristic magnetic anisotropy. The minority $[Y(Pc)(PcNO)]^{\bullet+}$ species is undetectable in these experiments, both due to its relatively small amount, but also due to its presumably similar relaxation characteristics to those of **2**.

These conclusions, did not address the discrepancy of the CW vs FSED spectra. We therefore considered that different resonances corresponded to transitions within multiplets of different total spin S_T, thus being characterized by different tipping angles. In the past, this had been explicitly examined in a copper(II)-nitroxyl radical complex, whose FSED spectra collected with pulses of varying B_1 demonstrated different spectral profiles.[37] Indeed, it was shown that within the spin system, singlet-triplet and triplet-triplet transitions were characterized by different tipping angles, the former tending toward an $S=0$ effective spin state, and the latter tending to an $S=1$ such state.

FSED experiments using pulses of the same durations ($t_{\pi/2} = 16$ ns) and different powers demonstrated this effect as shown in Figure 5. Indeed, while the $g=2.014$ resonance remains dominant, a resonance at $g=2.023$ disappears upon increasing MW powers, and a resonance at $g=2.028$ increases in its place. Similarly, on the high-field side of the spectrum, a resonance at $g=2.004$ disappears in favor of one at $g=2.000$.

To demonstrate that the two resonances at $g=2.0023$ and 2.0028 corresponded to transitions of different spin multiplicities, hence of different Rabi frequencies, we recorded the nutation traces of **2** at 6 dB at the corresponding magnetic fields. The FT spectra clearly show two peaks at 18.0 and 23.4 MHz, as well as a low-frequency peak at 14.65 MHz assigned to ^1H ESEEM modulations (see below for assignments). The relative increase of the high-frequency component at lower magnetic fields indicated that different resonances became more or less dominant as a function of field.

To corroborate the assignments of these peaks we carried out variable-power studies at the main peak ($g=2.014$) and at one of the minor peaks ($g=2.0023$). In each case, these experiments (Figure S21) revealed the presence of two Rabi oscillations, whose frequencies varied linearly with B_1, as well as a third, power-independent oscillation near 15 MHz, which we assigned to ^1H ESEEM (Figures S23 and S24).

For a more complete assessment of the spin states corresponding to different resonances, we carried out Field-Swept Spin Nutation (FSSN) experiments over the entire magnetic field range. Based on the previous variable-power experiments, we chose a MW power level where the Rabi
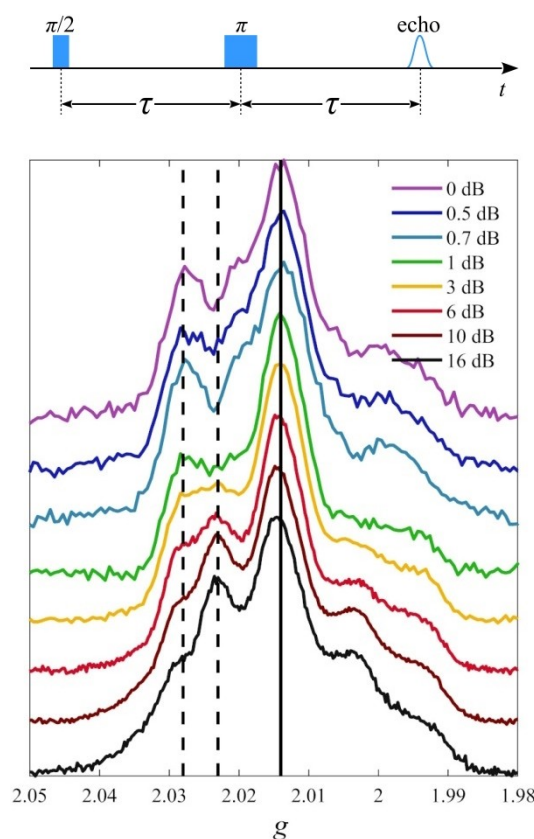

Figure 5. FSED spectra of **2** at 90 K and at different pulse intensities. The vertical continuous line shows the $g=2.014$ (345.1 mT) main absorption and the dashed ones the power-dependent absorptions at $g=2.023$ (343.7 mT) and $g=2.028$ (342.7 mT). Detailed nutation experiments were conducted on the $g=2.014$ and 2.028 absorptions (Figures S23 and S24, respectively). Experimental parameters: $f_{EPR}=9.72721$ GHz, $\pi/2$ pulse $=16$ ns, $\tau=454$ ns. The 0 dB spectrum corresponds to a MW field B_1 of 1.1 mT.

oscillation frequencies would be well separated from the ^1H ESEEM frequency; a 4 dB attenuation yielded satisfactory results. The pulse duration of the Hahn-echo detection block was appropriately set to $t_{\pi/2}=12$ ns.

Selected nutation traces and their FT spectra are shown in Figure 6. Fits were carried out to a model considering three exponentially damped oscillations, a power-independent one around 15 MHz, corresponding to the ^1H ESEEM, and two power-dependent ones assigned to Rabi oscillations, according to $M_z(t) = M_0 \sum_{i=1}^{3} k_i \cdot e^{t/\tau_{R_i}} \cdot \cos(2\pi f_{R_i} t + \varphi_i)$, where M_0 is the initial magnetization, f_{Ri} are the oscillation frequencies, k_i their relative amplitudes, τ_{Ri} their characteristic damping times and φ_i their phases. The field dependence of best-fit parameters is shown in Figure 7.

It is interesting to note that the oscillation amplitudes k_i. demonstrated remarkable correlation with FSED spectra. Indeed, while the low-frequency oscillation was dominant at all magnetic fields, it demonstrated amplitude maxima at $g=2.028$ and 2.014 and 1.995 and minima at $g=2.023$ and 2.003. The amplitude of the high-frequency oscillation showed the inverse behavior as a function of field, which is reasonable as the k_i amplitudes are correlated.
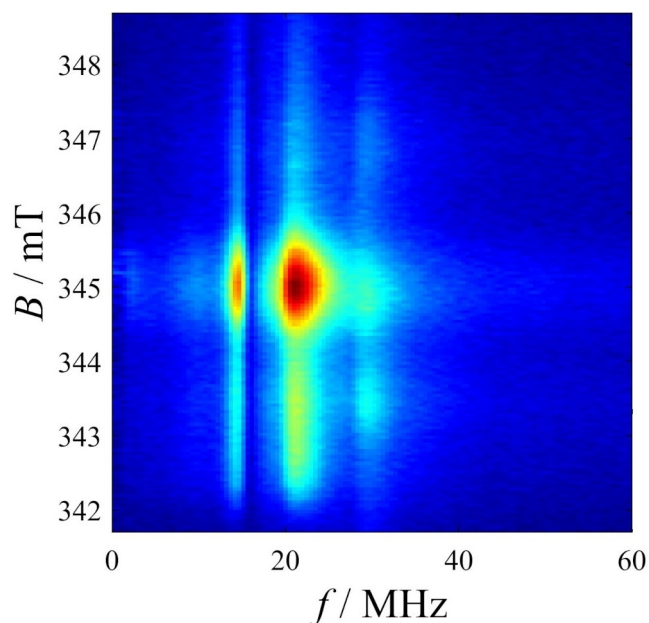
Chemistry–A European Journal

Research Article
doi.org/10.1002/chem.202400420

Chemistry Europe
European Chemical
Societies Publishing

Figure 6. Variable-field FT spectra of the nutation traces of **2** at 20 K. The
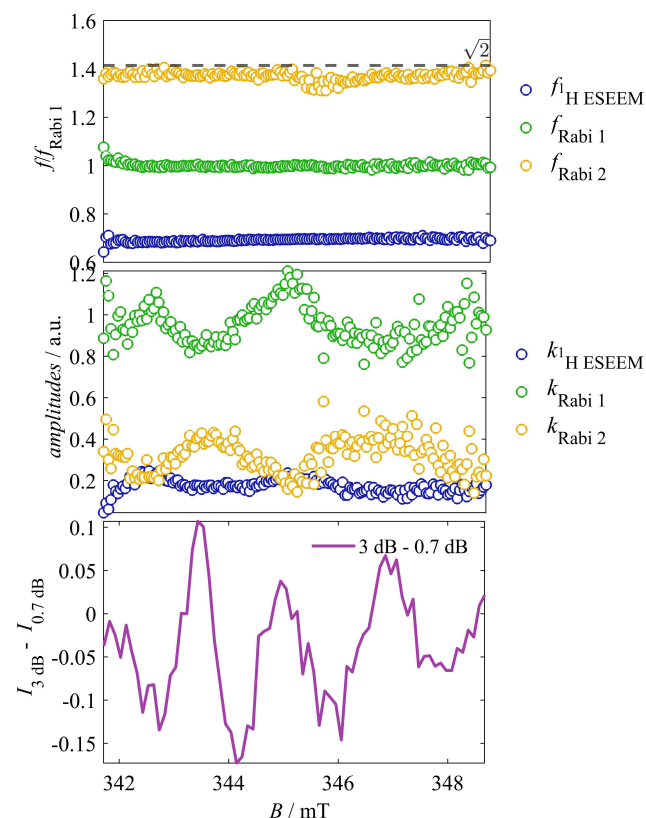

Figure 7. Top and middle panels: Magnetic field dependence of the frequencies (relative to the "$S = 1/2$" frequency) and relative amplitudes of the three oscillations. The horizontal dashed line in the top panel indicates the theoretical $\sqrt{2}$ frequency ratio between pure $S = 1$ and $S = 1/2$ spins. Bottom panel: Difference between the 3 and 0.7 dB FSED spectra. Maxima show resonances whose flip angles are such that they become suppressed at higher MW powers.

These correlate precisely with the MW power enhancements/suppressions of the FSED spectra. By subtracting the 0.7 dB spectrum from the 3 dB spectrum, we get corresponding maxima at the resonances suppressed at higher powers and minima at the resonances suppressed at lower powers (Figure 7, bottom panel). Therefore, there is a direct correlation between the shape of the FSED spectra and the relative amplitudes of the Rabi oscillations in FSSN experiments.

2.5. Distance Determinations from Nutation Spectroscopy

From the fits above, Rabi oscillation frequencies were found to be constant, at 29.35(35) MHz and 21.35(19) MHz, revealing different spin characters. In particular, their ratio was equal to 1.37, i.e. very close to, but not exactly equal to $\sqrt{2}$. This latter value would theoretically correspond to transitions within "$S = 1$" and "$S = 1/2$" multiplets, respectively, according to the relation:[38,39]

$$f_{nut} = \frac{\mu_B g_1 B_1}{h} \sqrt{S(S+1) - M_S(M_S+1)} \qquad (1)$$

where g_1 is the g-tensor element along the laboratory x-axis and B_1 is the strength of the excitation magnetic field. This relation is directly applicable only to intramultiplet transitions occurring in single-spin systems, or multispin systems with strong J couplings, where we assume that S and M_S are good quantum numbers. In the case of hyperfine interactions and admixtures of nuclear states, or in the case of diradicals with $J \sim \Delta g \mu_B B_0$, these conditions no longer hold,[38] necessitating further refinements.[40]

In our intermediate case, where $J \sim A_{HF}$ and $J \gg \Delta g \mu_B B_0$, this relation is not expected to hold, which is precisely what is observed. Treatment of Rabi frequencies in such systems provides a tool to probe weak terms such as dipolar, hyperfine and exchange interactions and g-asymmetries.

For the simplest of those cases, i.e. a symmetric ($\mathbf{g}_1 = \mathbf{g}_2$) diradical with $J \sim 0$, no hyperfine interactions and just moderate dipolar interactions ($r_{12} \sim 16$ Å),[41] two Rabi frequencies above certain B_1 intensities were predicted, corresponding to on- and off-resonance excitations, though field-swept nutation studies in that work only revealed one such frequency due to the weak interactions and symmetric **g** tensors. Moreover, this theory predicted that these frequencies will diverge from the predicted frequencies, under the influence of dipolar-induced anisotropy. Finally, Δg effects were predicted to enhance this departure in the case of g-asymmetry, in which case J-coupling should also become an influencing factor. This prompted us to attempt to analyze the ratio of two Rabi frequencies within the context a system experiencing a dipole-induced zfs,[41] thereby allowing us to propose a rationalization of our observations.

In a dipole-dipole interaction within a spin system of isotropic $S = 1/2$ spins, the dipolar interaction tensor $\mathbf{D}_{12}$ induces a zfs in the $S_T = 1$ state equal to $D_{12(zfs)} = 3\mathbf{D}_{12(zz)}/2$ which leads to an energy splitting of $\Delta E_{S=1} = D_{12(zfs)}/2$. Since the latter is related to the interspin distance by the empirical relation $\Delta E_{S=1} = \beta^2 g^2/$

r_{12}^3 ($\beta^2 = 12980$ MHz/Å^3 or 0.43297 cm^{-1}/Å^3), we have a direct means to correlate the triplet state's zfs to the interspin distance.

In particular, considering the power attenuation of the experiment (4 dB corresponding to $B_1 \sim 0.66$ mT) we constructed a curve of calculated Rabi frequency ratios as a function of $D_{12(zfs)}$ (Figure 8, left), in which the 1.37 ratio corresponded to a $D_{12(zfs)} \sim 53.7$ MHz. Assuming the simplified relation of the point-dipole approximation $D_{12(zfs)} = \beta^2 g^2 / 2r_{12}^3$ this energy yields a distance of $r_{12} \sim 7.85$ Å (Figure 8, right). Whilst the simplifications of the above model and of our treatment only allow for its qualitative use, it is quite remarkable that the predicted distance falls near the middle of the range of interspin distances based on the calculated structure of **2**, i.e. 6.5–12.5 Å.
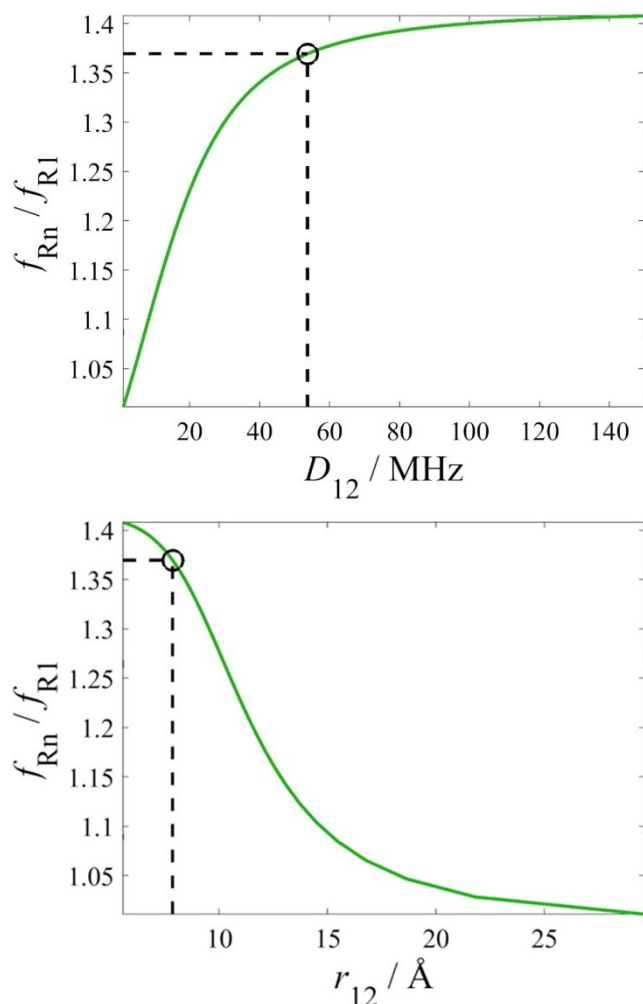

Figure 8. Ratio of the Rabi frequencies calculated for different dipolar interaction strengths (top) and the corresponding distances based on the point-dipole model (bottom). The dashed lines indicate the dipolar zfs and corresponding distance for the experimentally determined ratio of 1.37 (53.7 MHz, 7.85 Å).

3. Discussion and Conclusions

This work was initially motivated by our desire to synthesize a weakly coupled diradical with an engineered g-asymmetry. This effort was indeed successful, resulting in a system containing two distinctly different spins, characterized by weak super-exchange coupling ($|J| \sim 420$ MHz/0.014 cm^{-1}). However, our attempts to interpret the frozen-solution CW EPR spectra were hampered by two factors. First, the simultaneous presence of exchange and hyperfine couplings of comparable strengths creating a closely-packed spin ladder giving rise to a multitude of closely spaced transitions. Second, the strong spin delocalization over the phthalocyanine rings invalidating the point-dipole approximation. The above are detailed in the SI (Section 5.5 and Figure S25).

Subsequent attempts to provide a detailed characterization of our system led us to a series of realizations. First, we confirmed the uniqueness of T_1 and T_M times, concluding that our diradical behaved as a collective spin system. Second, variable-power FSED spectra and FSSN studies revealed resonances between states of different spin multiplicities, hence of different tipping angles. While this is a known attribute of g-asymmetric spin-coupled systems,[37,42] variable-power FSED experiments have been mostly used for analytical purposes, in particular the deconvolution of multicomponent spectra.[43] Similarly, the use of FSSN experiments has been developed as a complement to PELDOR in assessing dipolar interactions, yet still remaining extremely rare and resting on visual inspection of the respective FT spectra.[41,44]

With analytical objectives still in mind, we initially sought to gain a deeper understanding of the behavior of **2**. Thus, careful fits of the nutation traces, revealed information on frequencies, amplitudes and decay times, which demonstrated that the "$S = 1$" Rabi frequency is influenced by a dipolar-induced zfs of 53.7 MHz, corresponding to a distance of 7.85 Å.

An overview of the results from our analytical attempts is shown in Table 1.

Beyond their purely analytical objective, these fits also revealed two distinct Rabi frequencies (plus a ^{1}H ESEEM one), whose relative amplitudes at a given MW power were a function of the magnetic field. These conclusions were directly correlated to variable-power FSED experiments, which showed

Table 1. Overview of the spin Hamiltonian parameters of **2** determined by the experiments in this work.

Parameter	Value	Experiment
$g_{NO(iso)}$ [a]	2.0060	Fluid solution EPR
$A_{N-NO(iso)}$ [a]	40.74 MHz	
$A_{H-NO(iso)}$ [a]	0.67 MHz	
$g_{pc(iso)}$ [a]	2.0023	
J [b]	420 MHz	
$D_{12(zfs)}$	53.7 MHz	FSSN

[a] Values taken from the minor monoradical species and fixed during simulations. [b] Simulation value derived from the model described in the text (Section 3.3) and the SI (section 5.2).

Chemistry–A European Journal

Research Article
doi.org/10.1002/chem.202400420

Chemistry Europe
European Chemical
Societies Publishing

that resonances at specific fields could be selectively enhanced or suppressed as a function of MW power.

Overall, these results demonstrated a system characterized by two distinct transitions, capable of being driven at desired amplitudes by proper selection of magnetic field and/or MW power. In that respect, diradical **2** is reminiscent of a spin qutrit, although it might more accurately be described as a moderately coupled two-qubit system. It is to be noted that in our experiments the MW pulses were of the same frequency. Use of two different frequencies, e.g. such by mixing the primary MW frequency with frequencies from an Arbitrary Waveform Generator, should produce even more selective excitations and fine-tuned control of our qutrit.

From the perspective of molecular spin qubits, this work demonstrated that molecular-engineered diradicals can be used in different contexts. In the weak-exchange limit, diradicals may be useful to implement individually addressable two-qubit gates. These can be stable,[12] or photogenerated transient ones.[7] In the strong-exchange limit, diradicals form triplet states which may be used for implementations of qutrits. Already, the formation of transient triplet states through photo-excitation has been proposed for implementing qutrits.[45]

While this work was not focused on the optimization of the decoherence properties of **2** (e.g. by ligand deuteration, very low temperatures, dynamic decoupling sequences etc), we note that these actually compare quite well with those of other stable diradicals or photoexcited triplet systems, as shown in Table 2.

From our studies we demonstrated that diradical **2** is situated between these limits, with an additional complication stemming from the hyperfine interaction creating a closely-packed spin ladder. Under that light, specific design elements need to be revised to derive systems of increased utility. We are therefore in pursuit of two directions regarding molecular design. The first is to replace the nitroxide by a spin carrier lacking hyperfine interactions, thereby simplifying the addressing of the two-spin system. The second one is to introduce a linker between the two radicals such as an acetylene,[17] phenyl linker, or aliphatic linker since spin-spin interactions are critical parameters in experiments which demonstrate the CNOT gate operation.[7] Finally, apart from molecular design efforts, we are currently designing experimental protocols with multifrequency control of the spin qutrits.

These future synthetic endeavors will be based on the double-decker motif, which affords great facility of single-molecule experiments such as spin-transport,[13,14] STM Kondo measurements,[47,48] or STM EPR,[49] which will be employed to study individual molecules derived from this line of research.

Conflict of Interests

The authors declare no conflict of interest.

Data Availability Statement

The data that support the findings of this study are available from the corresponding author upon reasonable request.

Table 2. T_1 and T_M times of indicative diradical or spin triplet systems (stable or photoexcited), compared with those of **2**.

System	T_1 (ms)	T_M (µs)	Reference
bis-TEMPO		6.89 (50 K)	[12]
PTEMPO[a]	57 (10 K)	3.2 (10 K)	[46]
$(TTF^+)^\bullet$-(pyromellitimide$^-$)$^{\bullet[b]}$		2.6 (5 K)	[7]
$[Y(Pc)_2]^\bullet$	$\sim10^3$ (10 K)	8 (40 K)	[17]
C_{70} ($S=1$)[b]	3–5 (5 K)	13–20 (5 K)	[45]
2	13 (20 K)	14 (20 K)	This work
	0.4 (90 K)	6.8 (90 K)	

[a] 4-propargyl-2,2,6,6,–tetramthylpiperidine-1-oxyl.[46] [b] Photoexcited species.

[1] D. P. DiVincenzo, *Fortschritte der Phys.* **2000**, *48*, 771–783.
[2] E. Moreno-Pineda, D. O. T. A. Martins, F. Tuna, *Electron Paramag. Reson.* **2021**, *27*, 146–187.
[3] M. R. Wasielewski, M. D. E. Forbes, N. L. Frank, K. Kowalski, G. D. Scholes, J. Yuen-Zhou, M. A. Baldo, D. E. Freedman, R. H. Goldsmith, T. Goodson, M. L. Kirk, J. K. McCusker, J. P. Ogilvie, D. A. Shultz, S. Stoll, K. B. Whaley, *Nat. Chem. Rev.* **2020**, *4*, 490–504.
[4] E. Moreno-Pineda, C. Godfrin, F. Balestro, W. Wernsdorfer, M. Ruben, *Chem. Soc. Rev.* **2018**, *47*, 501–513.
[5] J. M. Zadrozny, J. Niklas, O. G. Poluektov, D. E. Freedman, *ACS Cent. Sci.* **2015**, *1*, 488–492.
[6] A. S. Poryvaev, E. Gjuzi, D. M. Polyukhov, F. Hoffmann, M. Fröba, M. V. Fedin, *Angew. Chem. Int. Ed.* **2021**, *60*, 8683–8688.
[7] J. N. Nelson, J. Zhang, J. Zhou, B. K. Rugg, M. D. Krzyaniak, M. R. Wasielewski, *J. Chem. Phys.* **2020**, *152*, DOI 10.1063/1.5128132.

Chemistry–A European Journal

Research Article
doi.org/10.1002/chem.202400420

Chemistry Europe
European Chemical
Societies Publishing

[8] Z. Y. Wang, Y. Z. Dai, L. Ding, B. W. Dong, S. Da Jiang, J. Y. Wang, J. Pei, *Angew. Chem. Int. Ed.* **2021**, *60*, 4594–4598.

[9] M. Bataille, *Quantum Inf. Process.* **2022**, *21*, 1–33.

[10] M. Y. Volkov, K. M. Salikhov, *Appl. Magn. Reson.* **2011**, *41*, 145–154.

[11] S. Nakazawa, S. Nishida, T. Ise, T. Yoshino, N. Mori, R. D. Rahimi, K. Sato, Y. Morita, K. Toyota, D. Shiomi, M. Kitagawa, H. Hara, P. Carl, P. Höfer, T. Takui, *Angew. Chem. Int. Ed.* **2012**, *51*, 9860–9864.

[12] E. J. Little, J. Mrozek, C. J. Rogers, J. Liu, E. J. L. McInnes, A. M. Bowen, A. Ardavan, R. E. P. Winpenny, *Nat. Commun.* **2023**, *14*, 1–37.

[13] R. Vincent, S. Klyatskaya, M. Ruben, W. Wernsdorfer, F. Balestro, *Nature* **2012**, *488*, 357–360.

[14] S. Thiele, F. Balestro, R. Ballou, S. Klyatskaya, M. Ruben, W. Wernsdorfer, *Science* **2014**, *344*, 1135–1138.

[15] C. Godfrin, A. Ferhat, R. Ballou, S. Klyatskaya, M. Ruben, W. Wernsdorfer, F. Balestro, *Phys. Rev. Lett.* **2017**, *119*, 1–5.

[16] A. K. Boudalis, J. E. Olivares-Peña, E. Moreno-Pineda, A. Fediai, W. Wenzel, P. Turek, M. Ruben, *Chem. Commun.* **2021**, *57*, 11505–11508.

[17] N. Suryadevara, A. K. Boudalis, J. E. Olivares Peña, E. Moreno-Pineda, A. Fediai, W. Wenzel, P. Turek, M. Ruben, *J. Am. Chem. Soc.* **2023**, *145*, 2461–2472.

[18] A. G. M. Barrett, G. R. Hanson, A. J. P. White, D. J. Williams, A. S. Micallef, *Tetrahedron* **2007**, *63*, 5244–5250.

[19] N. Ishikawa, Y. Kaizu, *J. Phys. Chem. A* **2000**, *104*, 10009–10016.

[20] N. Sheng, R. Li, C. F. Choi, W. Su, D. K. P. Ng, X. Cui, K. Yoshida, N. Kobayashi, J. Jiang, *Inorg. Chem.* **2006**, *45*, 3794–3802.

[21] V. E. Pushkarev, L. G. Tomilova, V. N. Nemykin, *Coord. Chem. Rev.* **2016**, *319*, 110–179.

[22] K. S. Chan, K. W. Mak, M. K. Tse, S. K. Yeung, B. Z. Li, Y. W. Chan, *J. Organomet. Chem.* **2008**, *693*, 399–407.

[23] A. S. Micallef, R. C. Bott, S. E. Bottle, G. Smith, J. M. White, K. Matsuda, H. Iwamura, *J. Chem. Soc. Perkin Trans. 2* **1999**, 65–71.

[24] Y. Horii, S. Kishiue, M. Damjanović, K. Katoh, B. K. Breedlove, M. Enders, M. Yamashita, *Chem. A Eur. J.* **2018**, *24*, 4320–4327.

[25] N. Ishikawa, O. Ohno, Y. Kaizu, *Chem. Phys. Chem.* **1991**, *180*, 51–56.

[26] J. E. Nutting, M. Rafiee, S. S. Stahl, *Chem. Rev.* **2018**, *118*, 4834–4885.

[27] H. Konami, M. Hatano, N. Kobayashi, T. Osa, *Chem. Phys. Lett.* **1990**, *165*, 397–400.

[28] P. Zhu, F. Lu, N. Pan, D. P. Arnold, S. Zhang, J. Jiang, *Eur. J. Inorg. Chem.* **2004**, 510–517.

[29] J. P. Blinco, J. L. Hodgson, B. J. Morrow, J. R. Walker, G. D. Will, M. L. Coote, S. E. Bottle, *J. Org. Chem.* **2008**, *73*, 6763–6771.

[30] R. Bolton, D. G. Gillies, L. H. Sutcliffe, X. Wu, *J. Chem. Soc. Perkin Trans. 2* **1993**, 2049–2052.

[31] S. S. Eaton, D. L. DuBois, G. R. Eaton, *J. Magn. Reson.* **1978**, *32*, 251–263.

[32] R. Wilson, D. Kivelson, *J. Chem. Phys.* **1966**, *44*, 4445–4452.

[33] A. Lupulescu, M. Kotecha, L. Frydman, *J. Am. Chem. Soc.* **2003**, *125*, 3376–3383.

[34] A. Cernescu, T. Maly, T. F. Prisner, *J. Magn. Reson.* **2008**, *192*, 78–84.

[35] J. L. Du, G. R. Eaton, S. S. Eaton, *J. Magn. Reson. Ser. A* **1995**, *115*, 213–221.

[36] W. Moore, R. Yao, Y. Liu, S. S. Eaton, G. R. Eaton, *J. Magn. Reson.* **2021**, *332*, 107078.

[37] S. S. Eaton, G. R. Eaton, *J. Magn. Reson. Ser. A* **1995**, *117*, 62–66.

[38] A. Schweiger, G. Jeschke, *Principles of Pulse Electron Paramagnetic Resonance*, Oxford University Press On Demand, **2002**.

[39] A. V. Astashkin, A. Schweiger, *Chem. Phys. Lett.* **1990**, *174*, 595–602.

[40] H. Matsuoka, K. Sato, D. Shiomi, T. Takui, *Appl. Magn. Reson.* **2003**, *23*, 517–538.

[41] K. Ayabe, K. Sato, S. Nishida, T. Ise, S. Nakazawa, K. Sugisaki, Y. Morita, K. Toyota, D. Shiomi, M. Kitagawa, T. Takui, *Phys. Chem. Chem. Phys.* **2012**, *14*, 9137–9148.

[42] S. Bertaina, S. Gambarelli, T. Mitra, B. Tsukerblat, A. Müller, B. Barbara, *Nature* **2008**, *453*, 203–206.

[43] M. Brustolon, F. Tampieri, M. Marrale, A. Barbon, *Appl. Magn. Reson.* **2015**, *46*, 481–488.

[44] K. Ayabe, K. Sato, S. Nakazawa, S. Nishida, K. Sugisaki, T. Ise, Y. Morita, K. Toyota, D. Shiomi, M. Kitagawa, S. Suzuki, K. Okada, T. Takui, *Mol. Phys.* **2013**, *111*, 2767–2787.

[45] Y. X. Wang, Z. Liu, Y. H. Fang, S. Zhou, S. Da Jiang, S. Gao, *npj Quantum Inf.* **2021**, *7*, 32, DOI 10.1038/s41534-021-00362-w.

[46] L. Tesi, F. Stemmler, M. Winkler, S. S. Y. Liu, S. Das, X. Sun, M. Zharnikov, S. Ludwigs, J. van Slageren, *Adv. Mater.* **2023**, *35*, DOI 10.1002/adma.202208998.

[47] T. Komeda, H. Isshiki, J. Liu, Y. F. Zhang, N. Lorente, K. Katoh, B. K. Breedlove, M. Yamashita, *Nat. Commun.* **2011**, *2*, DOI 10.1038/ncomms1210.

[48] T. Frauhammer, H. Chen, T. Balashov, G. Derenbach, S. Klyatskaya, E. Moreno-Pineda, M. Ruben, W. Wulfhekel, *Phys. Rev. Lett.* **2021**, *127*, 123201.

[49] R. Kawaguchi, K. Hashimoto, T. Kakudate, K. Katoh, M. Yamashita, T. Komeda, *Nano Lett.* **2023**, *23*, 213–219.

RESEARCH ARTICLE

The diradical formed by functionalizing the yttrium(III)-phthalocyaninato radical with a nitroxide radical, is characterized by an engineered g-tensor asymmetry and a weak exchange coupling. Interestingly, its behavior is reminiscent of a spin qutrit, exhibiting two EPR transitions characterized by different Rabi frequencies and whose amplitudes can be selectively enhanced by proper choice of microwave power or magnetic field.

g_{Pc} = 2.0023 g_{NO} = 2.0060

$|J| \sim 0.014$ cm^{-1}

**g–asymmetry engineering
Weak coupling**
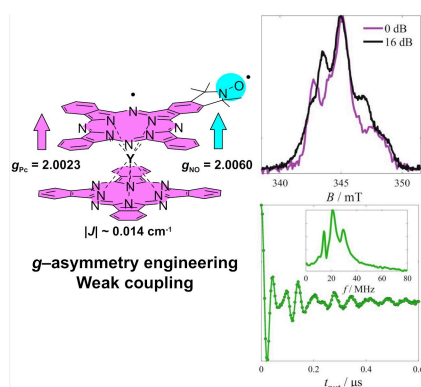
J. Komeda, A. K. Boudalis*, N. Montenegro-Pohlhammer, C. Antheaume, A. Mizuno*, P. Turek, M. Ruben*

1 – 11

Selective Transition Enhancement in a *g*-Engineered Diradical